Science Advances
AAAS

Supplementary Materials for

Vacuum ultraviolet nonlinear metalens

Ming Lun Tseng, Michael Semmlinger, Ming Zhang, Catherine Arndt, Tzu-Ting Huang, Jian Yang, Hsin Yu Kuo, Vin-Cent Su, Mu Ku Chen, Cheng Hung Chu, Benjamin Cerjan, Din Ping Tsai*, Peter Nordlander*, Naomi J. Halas*

*Corresponding author. Email: dptsai@cityu.edu.hk (D.P.T.); nordland@rice.edu (P.N.); halas@rice.edu (N.J.H)

Published 20 April 2022, *Sci. Adv.* **8**, eabn5644 (2022)
DOI: 10.1126/sciadv.abn5644

This PDF file includes:

Section I: Theoretical design of the meta-atom

The design of multifunctional metasurfaces includes several steps: selection of the constituent material, development of the meta-atom design, calculation of the required phase profile, and preparation of the metasurface layout. A summary of the process flow is shown in Figure S1. Zinc oxide (ZnO) was chosen as the nonlinear medium for the second harmonic generation (SHG) of 197-nm vacuum ultraviolet (VUV) light in this work. In our previous work, it has been shown that nanopatterned ZnO serves as a suitable artificial nonlinear device for SHG of VUV light (38). To realize a metasurfaces capable of both generating and controlling VUV light, several requirements in the meta-atom design need to be carefully tailored, including the resonance mode, structural symmetry, as well as the relationship of the localized phase versus the geometric parameters of a meta-atom. To achieve these multiple goals, we introduced two theories into the design of the meta-atom: the nonlinear selection rule and the nonlinear geometric phase (40). According to the selection rule for nonlinear media under circularly polarized illumination, the rotational symmetry of the meta-atom is only allowed to have certain values:

$$n = q \times l \pm 1 \quad \text{----------(1)}$$

Where n is the order of the nonlinearity, q is the rotational symmetry of the meta-atom, l is an integer. In our work, for SHG (n = 2) and the following consideration based on the nonlinear geometric phase, we chose the rotational symmetry (q) to be equal to three.

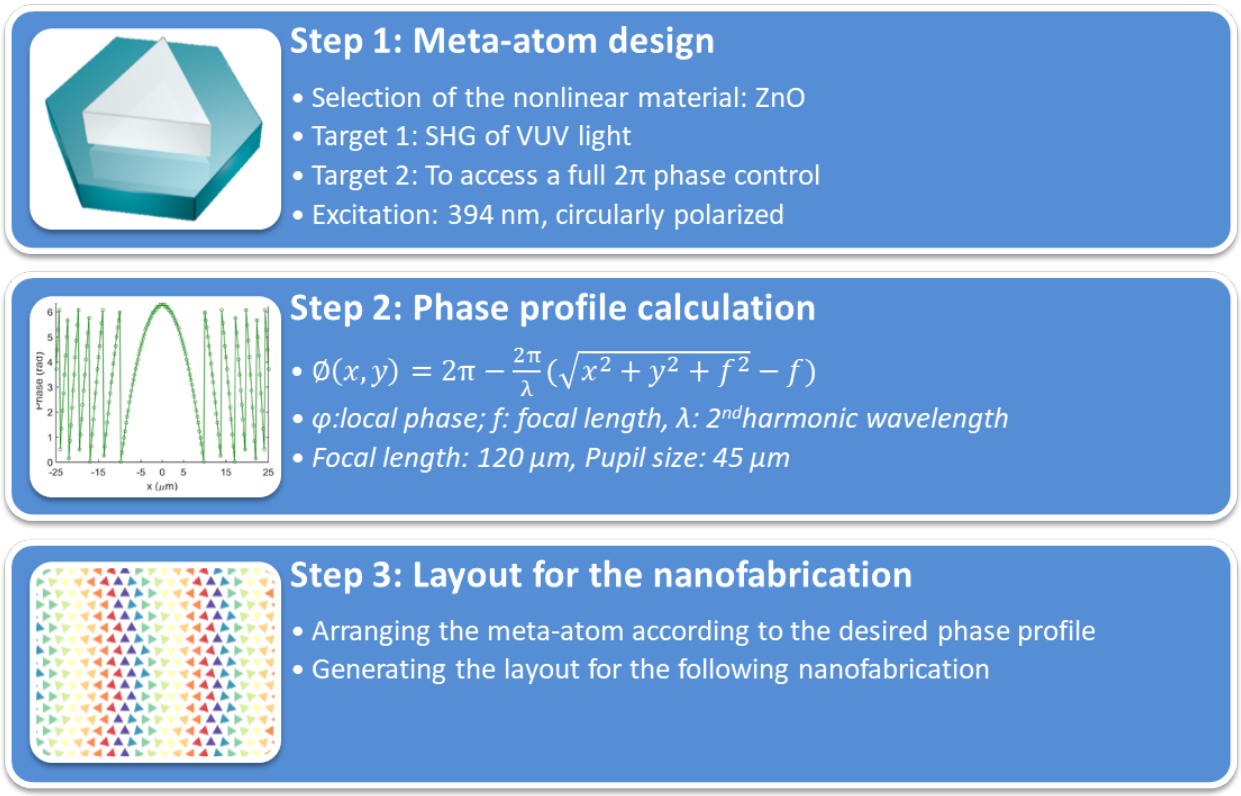

Fig. S1. Process for the design of the nonlinear metalens. The nonlinear metalens design can be divided into three main steps: design of the meta-atom, calculation of the phase profile for the targeted functionalities, and the preparation of the layouts.

To achieve full 2π phase modulation of the generated VUV harmonic wave, the concept of the nonlinear geometric phase was used. According to nonlinear geometric phase theory, under circularly polarized illumination, the nonlinear polarizability in meta-atoms with C3 rotational symmetry is proportional to $e^{(n+1)i\theta}$, where θ is the rotation angle of the meta-atom. Therefore, by combining the theories, we can access a full 2π phase control for the VUV light by gradually rotating the C3-symmetric meta-atom. Notably, although there are several C3-symmetric meta-atoms that have been used for SHG of visible light, including Y-shaped antennas and triangle-shaped holes, we chose nanotriangles as our unit cell. This is because they provide better field confinement inside the dielectric meta-atoms at the resonance, which boosts the light-matter interaction between the fundamental light and the nonlinear medium ZnO.

With the nonlinear selection rule and the nonlinear geometric phase requirements in place, the design of the meta-atom involves linear and nonlinear electromagnetic simulations using the Finite Element

Method (COMSOL multiphysics 5.4). The meta-atom was designed to exhibit a magnetic dipole resonance (Figure 1C in the main text) at the fundamental wavelength (394 nm) under circularly polarized illumination to provide field enhancement inside the ZnO nanotriangles.

The ZnO meta-atoms were modeled as triangular pillars with an edge length of 205 nm and a height of 150 nm. 10 nm rounding was added to the triangle corners in the xy plane. A circularly polarized plane wave excitation was propagated from the glass substrate side of the metasurface. Perfectly matched layers were applied in the vertical direction to prevent artificial reflection. To model a periodic meta-atom array, the simulation region was set to represent a unit cell of the hexagonal lattice. Periodic boundary conditions were also applied in the horizontal directions. The refractive index of soda-lime glass was set to be 1.5. We adopted the refractive index data of ZnO from the ellipsometry measurements (Spectroscopic Ellipsometer, HORIBA). As in our previous work (38), we multiplied the reported value of ZnO by a factor of 1.2 to account for the refractive index variation due to different preparation methods. A two-step method was used to calculate both the linear mode analysis and nonlinear transmission from the resonator array. In the first step, a linear simulation at the fundamental wavelength was performed to obtain the field profile within the ZnO nano-resonator under normal circularly polarized plane wave illumination from the glass side. The relative strength of the induced dipole moments contributing to the far field radiation was then calculated with a standard mode decomposition technique. In the second step, linear simulations with both left and right-hand circularly polarized (defined from source view) normal illumination, from the air side, were performed at the SHG wavelength. The field profiles of the nano-resonators at the fundamental and the second harmonic wavelength were then used to calculate the far field second harmonic emission for both handednesses following the Lorentz reciprocity theorem (5*1*). To obtain the relationship between the far-field second harmonic emission and the nano-resonator rotation, we rotated the resonators in the simulated array uniformly with eight different angles ranging from 0 to $2\pi/3$ and calculated the corresponding second harmonic emission phase and amplitude (Supplementary Table 1). However, in the previous investigation (38), the SHG of dielectric metasurfaces are found to be insensitive to the absorptive surrounding materials as the energy is strongly confined in the Mie-type nano-resonators at the fundamental and harmonic

wavelengths. In simulation, VUV light absorption in the soda-lime glass substrate and a refractive index shift for the substrate at 197nm have only a moderate effect on the performance of the metalens. Therefore, the *n* and *k* of the glass substrate are set as 1.5 and 0, respectively in the nonlinear simulation to accelerate the design process.

Supplementary Table 1. The rotational angle of the meta-atom versus the phase of the output VUV light (in degree)

Rotational Angle	Phase (theory)	Phase (Sim.)
0	0	0
15	45	55.4
30	90	95.1
45	135	131.2
60	180	180.0
75	225	235.1
90	270	275.2
105	315	311.3

The phase profile for the metalens were calculated according to different targeted functionalities. The lens formula, which can be described using the following formula, was used:

$$\varphi(r) = k_0(\sqrt{f^2 + r^2} - f)$$

Where *r* is the radial distance toward the center of the metalens (diameter: 45 μm), f is the designed focal length, k_0 is the wave vector ($2\pi/\lambda$), and λ is the second harmonic wavelength (197 nm).

Subsequently, the layout was prepared according to the simulation results and the phase calculation. The mask was divided into grids in a hexagonal lattice (lattice constant: 270 nm). The meta-atoms were placed into the grids and were rotated according to the required local phases.

Section II: Nanofabrication

The process flow used for the nonlinear metalens fabrication was similar to the one used in our previous work for the fabrication of gallium nitride metalenses(*52*). The process flow is presented in Figure S2. Sputtered zinc oxide (ZnO) thin films on soda-lime glass substrates were used for the nanofabrication. The thin films were purchased from MTI Corporation, USA. According to the documentation provided by MTI Corporation, the ZnO thin films have a thickness of 150 nm and average surface roughness of 0.435 nm. In addition, they are reported to be of polycrystalline nature with (002)-orientation. Plasma-enhanced chemical vapor deposition (PECVD, Samco Inc.) was used to deposit a 400 nm thick silicon dioxide (SiO_2) layer on top of the ZnO thin film. The sample was then coated with a 100-nm-thick resist ZEP-520A (Zeon Corp., Japan) on top of the SiO_2 layer, followed by coating an Espacer layer directly onto the resist-coated substrate in order to avoid the proximity effect coming from the electron scattering in the resist layer. E-beam writing was carried out using an Elionix ELS-7000 electron-beam lithography system. The acceleration voltage was 100 kV while the beam current was 100 pA. The development process was done by immersing the sample in ZEP-N50 (Zeon Corp., Japan). Subsequently, a 40 nm thick chromium (Cr) layer was deposited using an electron-beam evaporation system, followed by the lift-off process performed in a Dimethylacetamide solution (ZDMAC, Zeon Corp., Japan). After that, reactive ion etching (RIE, Samco Inc.) with an RF power of 90 W was used to transfer the pattern into the SiO_2 layer. Inductively-coupled-plasma reactive ion etching (ICP-RIE, Samco Inc.) was subsequently carried out using mixed BCl_3/Cl_2 chemistry (radio frequency: 13.56 MH_Z, ICP source power: 700 W, bias power: 280 W). Finally, the remaining SiO_2 layer was removed using the Samco Inc. RIE system. An SEM image of a resulting metasurface is shown in Figure S3.

To fabricate the beam steering metasurface, a 150-nm-thick ZnO thin film was coated with a 1 nm thick Cr layer via electron beam evaporation with a base pressure of less than $5x10^{-6}$ Torr. The Cr layer served as a conductive layer for the subsequent focused ion beam milling to avoid any potential charging effects that would affect the precision of the ion beam scanning. The designed metasurface was patterned into the thin film by using a dual-beam Gallium ion-based focused ion beam system (FEI Helios 660 NanoLab)(*53*). The acceleration voltage was 30 keV, while the beam current used in the fabrication was around 51 pA. The dose applied to the thin film was around 20 $\mu C/cm^2$. To well define the scanning path and the writing strategy of the Gallium ion beam, the NPGS software provided by JC Nabity Lithography Systems, USA, was used to precisely control the scanning path of the ion beam.

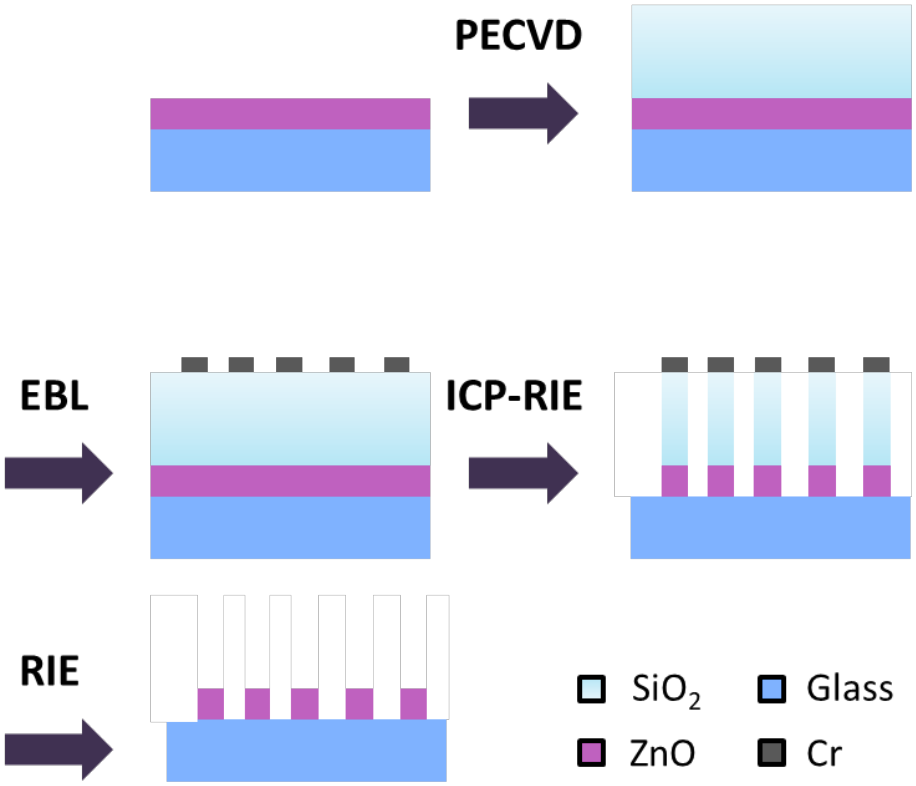

Fig. S2. Nanofabrication of the nonlinear metalens. The reported metalens was fabricated by performing PECVD and electron-beam lithography (EBL) on a sputtered ZnO thin film followed by several steps including inductively-coupled-plasma reactive ion etching (ICP-RIE) and reactive ion etching (RIE) processes.

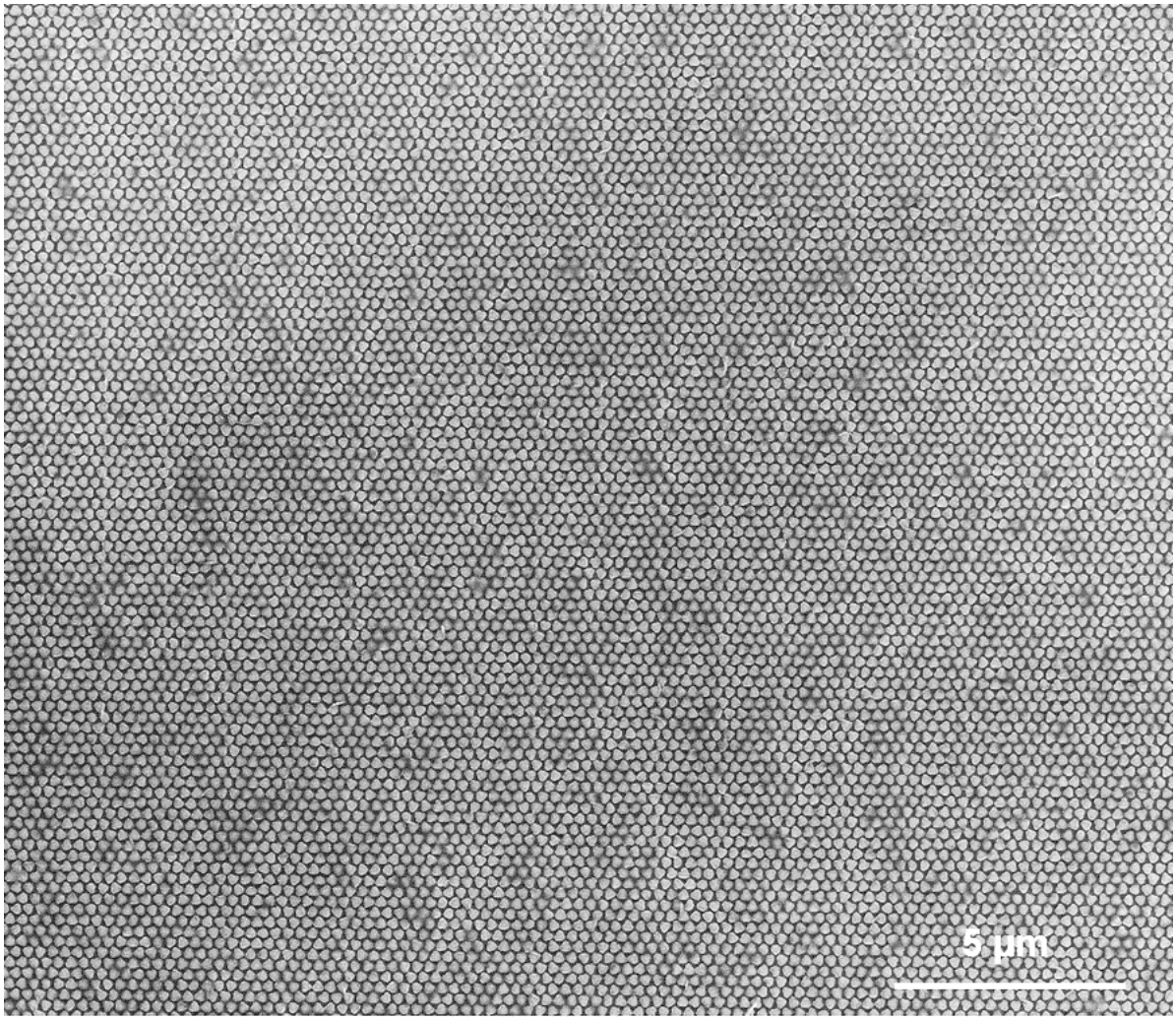

Fig. S3. SEM image of the resulting metasurface.

Section III: Measurements

Section III.I Linear measurements

The linear transmission measurement of the metalens was performed using a micro-spectrometer based on an inverted Olympus microscope IX-70, which has been used in our previous work(5*4*). A halogen light source was used for the excitation. The incident light was guided to the sample using a long working distance condenser. A broadband linear polarizer and a broadband quarter waveplate (Thorlabs) were

placed in the microscope to convert the polarization of the incident light into a circularly polarized state. A spectrometer box (B&W Tek, Inc., BTC111E) was mounted on the microscope for the spectral analysis.

Section III.II Focusing and beam steering measurements

The metalens focusing profile and beam steering measurements were performed with a custom-built setup that is shown in Figure 3A in the main text. Here, a more detailed schematic that includes more details about the laser system is shown in Figure S4. This figure also shows the relative placement of all three bandpass filters as they were used in the detection path, while Figure 3A in the main text shows them in a single symbol. Some key components of the setup are listed in the main text, while additional details are provided here. The laser system consisted of a mode-locked, ultrafast Ti:shappire laser (Coherent Mira) 900 that was pumped with a Coherent Verdi V5 (5 W) laser and served as a seed laser to a regenerative amplifier (Coherent RegA 9000) that was pumped with a Coherent Verdi V10 (10W). The beam from the amplifier was frequency doubled using a frequency doubling crystal in an optical parametric amplifier (Coherent OPA 9400) and guided into the setup. Note: the optical parametric amplifier was used for the frequency doubling step due to convenient availability, but it was used in a detuned fashion such that as little light as possible was lost to the other nonlinear processes within the optical parametric amplifier. A spatial filtering setup was used to improve the uniformity of the excitation beam.

As mentioned in the main text, the excitation laser was focused 2 mm before the metalens surface to produce a near-plane wave incident condition at the metalens surface. The Gaussian diameters of the laser excitation spot were measured to be about 126 μm and 139 μm, in the x- and y-direction, respectively, at the metalens z-position, which was 2 mm in the positive z-direction from the focus point of the excitation laser (see Figure 3A in the main text for a schematic that includes the excitation setup). A motorized stage was used to scan the detection setup and therefore allowed the nonlinear imaging of the metalens as well as the focusing spot of the VUV light. The experimental data presented in Figure 3 in the main text is from a scan with 2 μm target step intervals. The position of the stage was measured at each z position via a stage command. This measured z position varied up to 1 μm from the target position. The measured z positions were used in the data analysis. Gaussian fits of the cross-sections through the focusing spot of the harmonic

wave yielded beam waist diameters of 2.74 µm and 2.82 µm in the x- (Figure S5A) and y-direction (Figure S5B), respectively. However, as one camera pixel was calculated to correspond to an imaging width of 0.528 µm, the Gaussian beam waist diameter ($1/e^2$) was only reported as around 3 µm in the main text. The gaussian fit of the cross-section through the focusing spot in the z-direction yielded a beam wait radius of 20.9 µm (Figure S5C). However, due to the mentioned variation between the measured and targeted z position values and the accuracy and repeatability values of the motorized stage reported on the Newport website (typical accuracy: ±0.8 µm and guaranteed accuracy ±2.0 µm), the focusing depth ($1/e^2$ diameter) was reported to be around 40 µm in the main text.

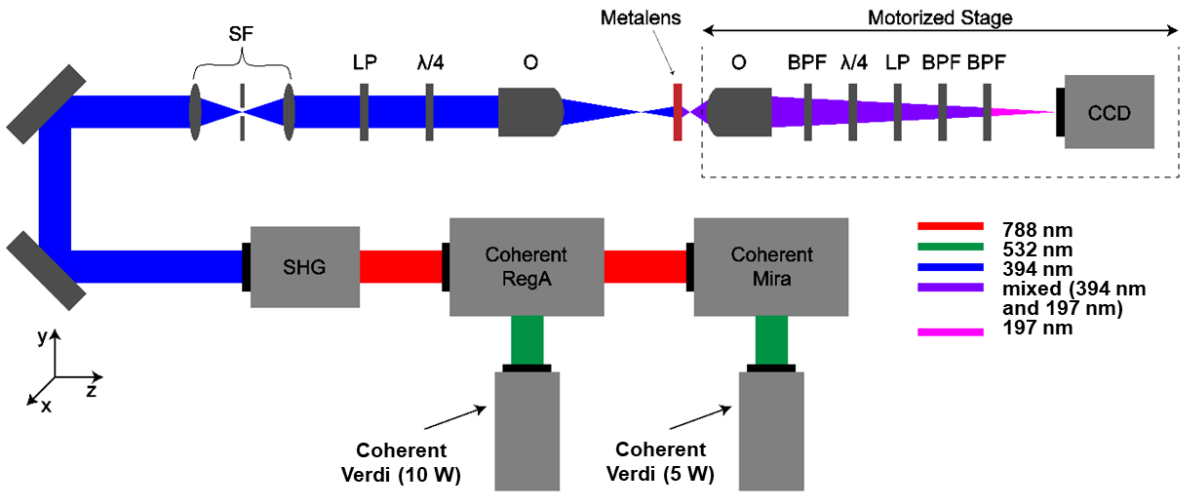

Fig. S4. Detailed experimental setup for the metalens and beam steering measurements. SF: spatial filtering setup, λ/4: quarter-wave plate, LP: linear polarizer, O: objective, BPF: bandpass filter.

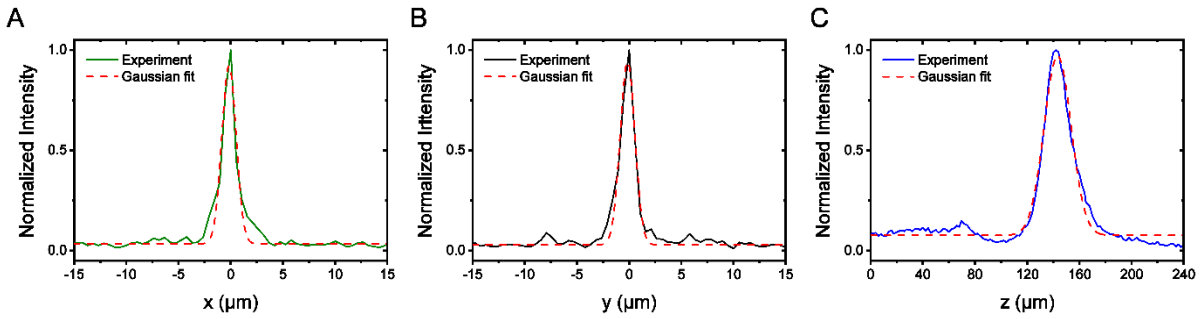

Fig. S5. Experimental cross-sections of the focusing spot. Cross-sections of the metalens focusing spot, including Gaussian fits in the (A) x-direction, (B) y-direction, and (C) z-direction.

Section III.III Nonlinear spectral measurement

The wavelength of the generated second harmonic signal was verified using a custom build setup (Figure S6). Partial pre-separation of the SHG from the fundamental (397.5 nm) was achieved by using a bandpass filter (Newport, 10LF20-193-B) as well as an equilateral dispersive calcium fluoride prism (Thorlabs, PS863), before focusing the signal into a monochromator (Thermo Jarrel Ash, 2400 grooves/mm grating). This was necessary to achieve a sufficient reduction of the fundamental signal. After the monochromator, the signal was detected using a photomultiplier tube (ADIT Electron Tubes, 9781B6019) that was in a chilled housing with a temperature below -10 ºC. Figure S7 shows a log-log plot of the SHG power of the metasurface compared to an unpatterned ZnO thin film with respect to incident pump power varied from 2.5 mW to 14 mW for the metasurface and 4 mW to 20 mW for the thin film. The peak power density was estimated based upon the temporal pulse width, repetition rate, and spot size of the fundamental beam. The metalens strongly enhances the SHG signal.

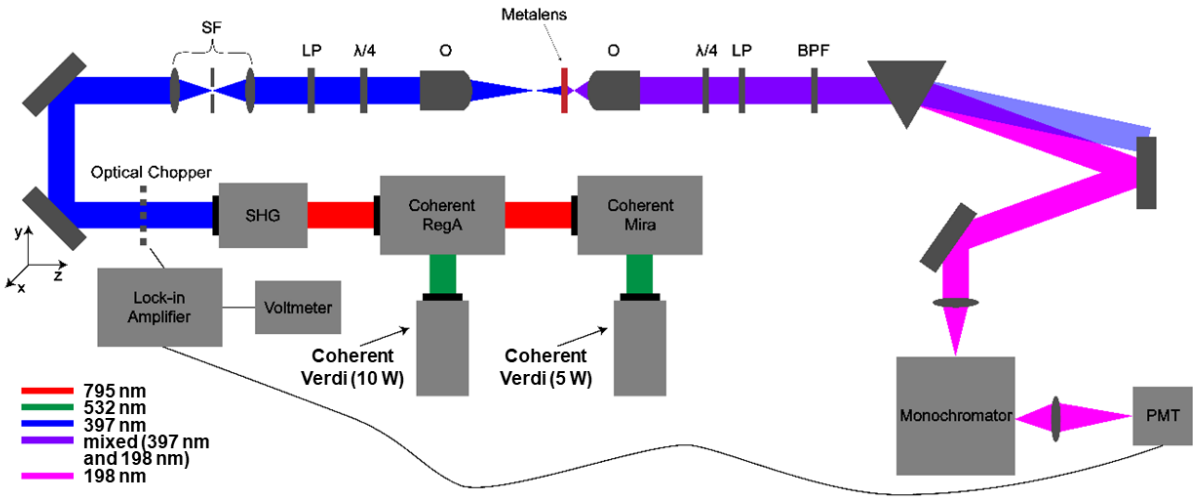

Fig. S6. Nonlinear spectral measurement. Schematic of the experimental setup. SF: spatial filtering setup, λ/4: quarter-wave plate, LP: linear polarizer, O: objective, BPF: bandpass filter.

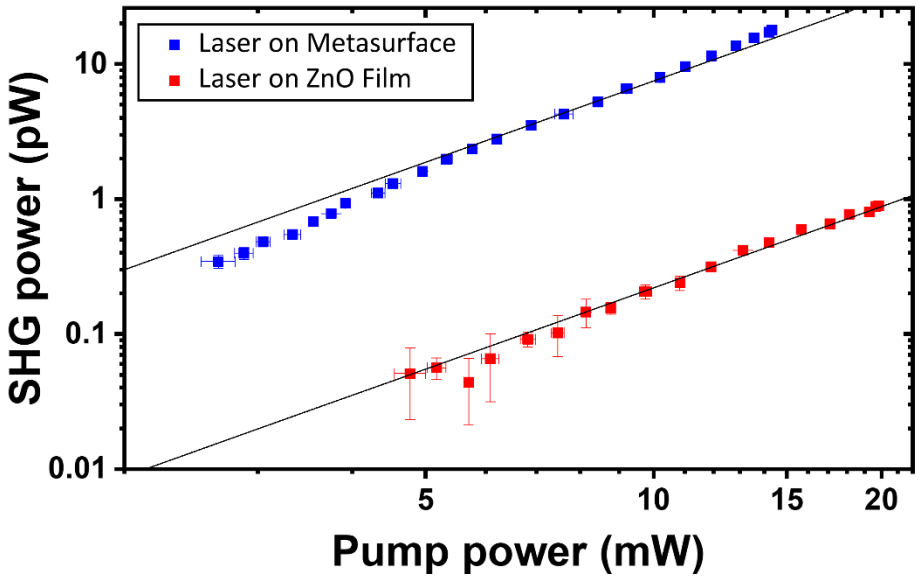

Fig. S7. SHG power dependence of metalens compared to the substrate. Black line: squared fit.

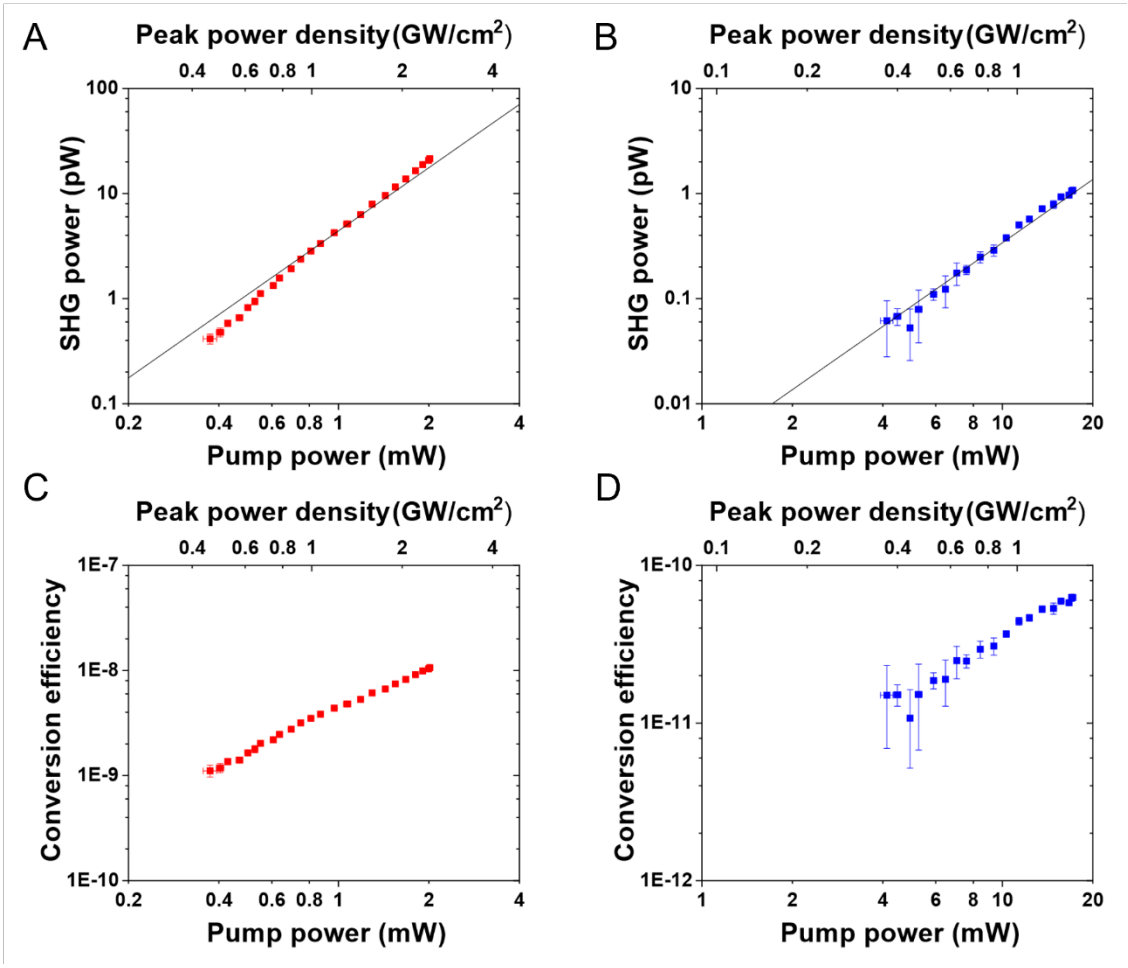

Fig. S8. Power dependence measurements. SHG power dependence of the a) metalens and b) surrounding ZnO thin film. Resultant conversion efficiency of the c) metalens and d) surrounding ZnO thin film.

Section IV: Focusing simulations

Section IV. I Light propagation simulations

The scalar-diffraction-theory-based light propagation simulations were performed with a self-developed Python module. We coded the metalens plane as a 50 μm by 50 μm cartesian field mask with a 0.01 μm grid interval. The metalens was coded as a circle with a diameter of 45 μm in the center of the plane. The meta-atoms on the metalens plane were modeled as perfect triangles with the same rotation as the design pattern. Grid points within the same meta-atom shared the same complex amplitude. We assumed that only the meta-atoms contribute to the far-field radiation from the metalens, i.e., all other areas on the

metalens plane were assigned an amplitude of zero. The incident light of the system was modeled as a spherical wave from a point light source 2 mm before the metalens with a maximum amplitude of 1. The mask was then multiplied with the incident light field to obtain the wavefront after the light passing through the metalens. The electric field distribution on the target plane was calculated with Kirchhoff's diffraction formula. The orthogonal electric field components, E_x, E_y, and E_z of the incident light were processed separately. The total light intensity was then obtained by calculating the sum over the square of the modulus of the three electric field components. Fast Fourier Transforms were used to speed up the calculation. To eliminate the higher-order diffractions, which were not collected in the experiment, we placed a virtual monitor plane 50 μm behind the target plane that is of the same NA as the objective used in the experiment. The light intensity on a target plane was calculated by first propagating the light to the virtual monitor plane and then back-propagating it to the target plane. In the simulation, with the perfect shape of geometry and full area contribution of the given metalens design, the enhancement of the VUV power density at the focus spot can be up to 2500-fold compared to the power density at the metasurface plane. However, it is challenging to achieve such an enhancement value with our current metalens samples. Possible reasons can be associated with local defects inside the multi-crystalline ZnO film used for the metalens and sample imperfections caused in the fabrication process. Both effects can lead to a reducing in the ability of the metalens to focus the VUV light, since nonlinear processes are highly sensitive to the uniformity of the meta-atoms. In the future, multiple strategies can be used to minimize imperfections and further improve nonlinear metalens performance, including increasing number of meta-atom, improving the nanofabrication process, and introducing novel nonlinear materials in the designs to achieve more precise VUV light generation and wave control.

Section IV.II Simulated focusing with different metalens amplitude and phase coding

To investigate the tolerance of light focusing capability of the nonlinear metalens in the presence of imperfect unit cells, we performed a series of light propagation calculations with different metalens encodings. In this way, we studied the effect of errors in the local phase and amplitude on the focusing capability of the metalens. Three different encoding methods were tested. These were: the ideal encoding

where all the cells are fully transparent and introduces a phase shift equals to three times the corresponding geometric rotation of the nanotriangle meta-atom (perfect encoding); the encoding following the rotation-amplitude and rotation-phase shift relationship used to generate Figure 1E (simulated encoding) in the main text; and an encoding that adds random phase and amplitude errors within certain ranges to the perfect encoding for each cell (random encoding). Here, we used two different sets of ranges for the random encoding: the first calculation (Figure S8 E, F) has a phase error range of $[-\pi/12, \pi/12]$ and an amplitude error range of [-0.25, 0.25]. The second calculation (Figure S8 G, H) has a phase error range of $[-\pi/2, \pi/2]$ and an amplitude error range of [-0.5, 0.5]. According to the simulated focusing profiles (Figure S8), perfect encoding (Figure S8 A,B), simulated encoding (Figure S8 C,D), and random encoding with relatively small errors (Figure S8 E,F) all focused the incoming light at around $z = 124$ μm and have similar intensity distributions on the focal planes. The focusing effect starts to degenerate only when the metalens has significant random errors (Figure S8 G,H). Compared to the cases presented in Figure S8 B (the ideal metalens) and Figure S8 H (metalens with phase and amplitude defects), the power density enhancement decreases by around 60%. However, while the focusing ability of the metalens is clearly affected by this error, the center of the focusing region remains remarkably tolerant. This result shows that our geometric-phase-based metalens design is of high tolerance against amplitude and phase variance.

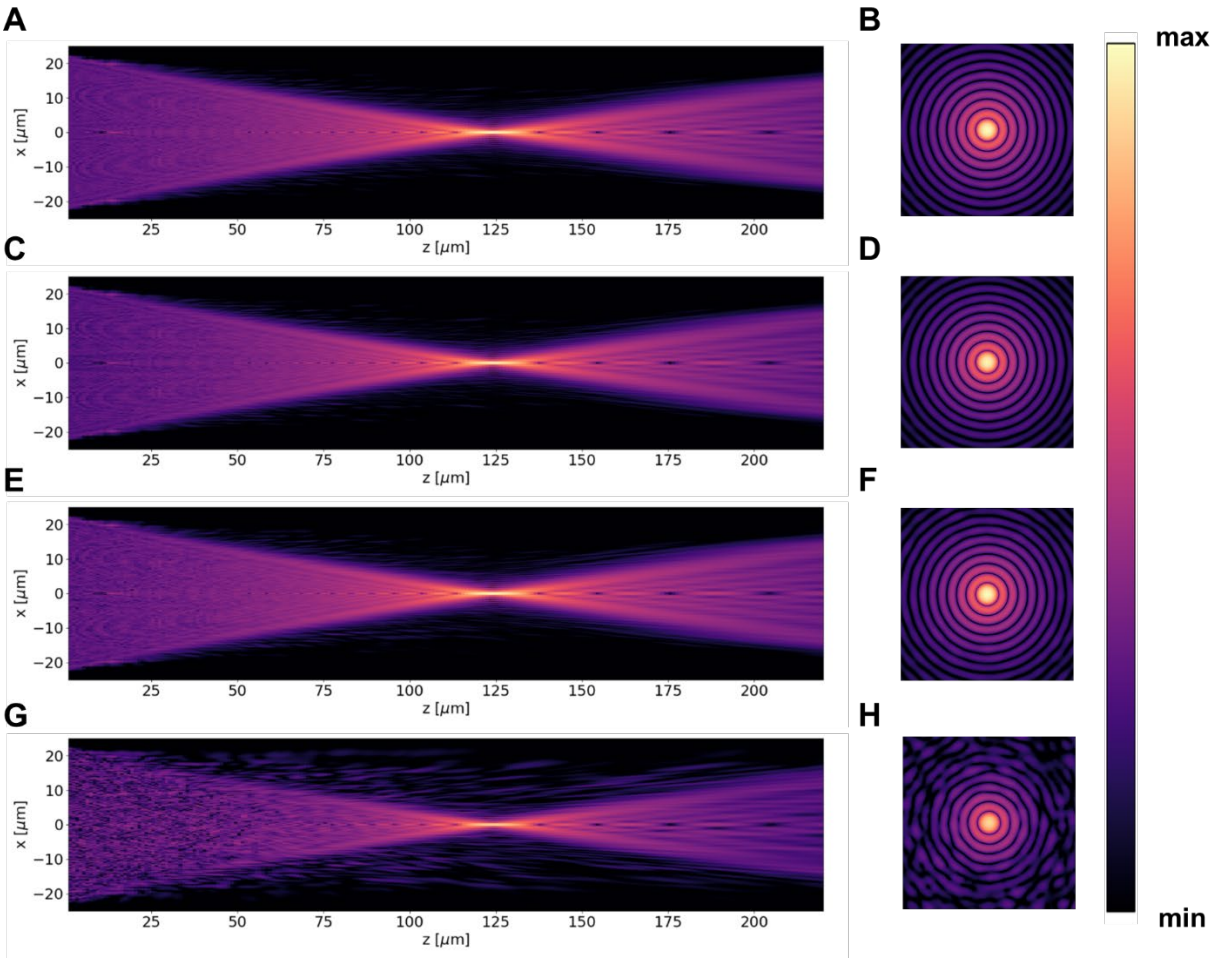

Fig. S9. Simulation of the metalens focusing profiles with different metalens encodings. Logarithmic focusing profile for the xz plane and 5 μm by 5 μm xy plane at z = 124 μm for (A, B) perfect metalens encoding, (C, D) simulated metalens encoding, (E, F) random metalens encoding with a phase error of [-π/12, π/12] and an amplitude error of [-0.25, 0.25], and (G, H) random metalens encoding with a phase error of [-π/2, π/2] and an amplitude error of [-0.5, 0.5]. All the plots share the same color scale.

Section V: Computation of power density values

The power density values were all computed using custom MATLAB code. Several methods, discussed below, were used to select pixels used to calculate the average power. For all calculations, the average power was calculated by converting total counts to photons, accounting for the quantum efficiency and integration time of the camera, and finally dividing by the transmission of the optical components between the metasurface and the camera CCD. The average power density is the average power divided by the total area of the pixels used to compute the average power. Peak power is computed by dividing the average power by the repetition rate of the laser and pulse width of the second harmonic light. The pulse width of the second harmonic light was determined from the pulse width of the excitation laser multiplied by a temporal conversion factor of $1/\sqrt{2}$ to account for the shorter pulse width of the generated light(55). Peak power densities were calculated by dividing the peak power by the total area of the pixels used to calculate the average power. These calculated values may be found in Supplementary Table 2 for cross-polarized SHG.

Supplementary Table 2. Power Density Analysis Values – Cross-polarized SHG

	Area of Integration (cm^2)	Radius of Integration Boundary (μm)	Threshold	Average Power (W)	Average Power Density (W/cm^2)	Peak Power (W)	Peak Power Density (W/cm^2)	Focusing Efficiency	Number of Integrated Pixels
Brightest Pixel	2.78E-9	N/A	N/A	9.80E-14	3.52E-5	2.71E-6	9.72E2	0.39%	1
Focal Plane (50%)	1.39E-8	N/A	50%	3.64E-13	2.61E-5	1E-5	7.21E2	1.5%	5
Focal Plane (10%)	2.89E-7	N/A	10%	1.94E-12	6.69E-6	5.35E-5	1.85E2	7.7%	104
Surface	1.34E-5	21.1	10%	2.50E-11	1.87E-6	6.90E-4	51.5	N/A	4812

Section V.I Terms Defined

Brightest pixel: The brightest pixel from the raw camera data was singled out and used to compute the values.

Focal plane: To determine the pixels on the CCD corresponding to the focusing plane of the metasurface, thresholds of 10% of the maximum signal and 50% of the maximum signal (FWHM) were used. The number of pixels that fell completely within the radius of integration are listed in the far right column. The pixels are oriented in a circular configuration within the circular area of integration. See "Power density at the surface" section for more information regarding the algorithm techniques.

Power density at the surface: To determine the pixels on the CCD corresponding to the surface of the metalens, a threshold of 10% of the maximum signal was used, identical to that discussed above, to determine the boundary of a circular integration area. However, the 10% threshold eliminated a significant number of pixels within the integration area corresponding to weaker signal from the metasurface. Therefore, the threshold selection only served to define the boundaries of a circular area of integration. The horizontal difference between the farthest right pixel and farthest left pixel corresponded to the horizontal diameter of the circular integration area. Similarly, the vertical diameter was calculated. However, the vertical diameter severely underestimated the size of the metasurface because several pixels fell outside of the threshold. The center of the integration area was defined as the pixel which was at the intersection of the vertical and horizontal diameters. However, only the horizontal diameter was used as the diameter of circular integration area for the calculated values due to more consistent signal across the horizontal axis of the metasurface image. The resulting diameter and integration area may be found in Supplementary Table 2. Pixels which fell partly outside of the integration area boundary were excluded from the calculations. Only accounting for full pixels resulted in less than 1.1% difference when compared to the full circular area. Therefore, only pixels which fell completely within the boundary of the circular region of integration were used to compute the average power and total integration area.

According to the nonlinear PB phase theory, the polarization of the generated SHG wave should be orthogonal to the polarization of the excitation. However, due to the sample imperfection, we found the polarization is not purely cross-polarized. The surface area of integration for co-polarized SHG is calculated to be 1.24×10^{-5} cm^2 with a 20.3 μm radius integration boundary with a 10% threshold. The average power at the surface is 3.67×10^{-11} W, average power density of 2.96×10^{-6} W/cm^2, peak power of 1.01×10^{-3} W, and peak power density of 81.7 W/cm^2. Therefore, the ratio between the cross- and co-polarized light is ~68%.

The focusing efficiency of the cross-polarized SHG is found to be about 7.7% when considering a threshold of 10% of the highest pixel intensity. However, according to the simulation, the focusing efficiency of the cross-polarized SHG is estimated to be ~ 75%. There could be multiple reasons for the discrepancy between the theoretical and experimental values. First, it is highly possible that the efficiency is underestimated due to the limited resolution of our detection optics. In principle, to analyze the focusing efficiency of a metalens, proper resolution of the detection system is needed to reconstruct the focusing profile for the data analysis. However, as high magnification objectives for the VUV range are not commonly available, the best objective can be found is a 15 × objective (Thorlabs LMU-15X-193). As a result, there are only ~5 pixels around the focusing spot at FWHM (threshold of 50% of the highest pixel intensity), which is not enough for accurate analysis of the focusing efficiency. Therefore, a threshold of 10% of the highest pixel intensity with 104 integration pixels was also considered.

Section VI: Nonlinear metasurface beam deflector

To further demonstrate the capability of the proposed approach to realize multifunctional VUV devices, we designed and fabricated a nonlinear beam deflector that can control the emission wavefront of the harmonic toward a specified direction. In the design, the orientation of the unit cells is assigned according to the following phase distribution(*56*):

$$\varphi(x, \lambda) = -\frac{2\pi}{\lambda} x \sin \theta_d,$$

where x is the spatial coordinate, θ_d is the refracted angle, and λ is the second harmonic wavelength, respectively. The deflection angle for the +1-diffraction order of the harmonic wave generated from the metasurface was designed to be nominally 8.5 degrees, while the -1-diffraction and zero-order will be suppressed. An SEM image of the resulting sample is shown in Figure S8A. ZnO meta-atoms with designed orientations, according to the theory, can be seen in the image. In the characterization, under normal excitation, a spot associated with the +1-diffraction order of the generated harmonic wave was observed, while the ones corresponding to the -1 and zero diffraction order are significantly weaker (Figure S8B). A cross-section of the corresponding angular dependence of the SHG intensity is plotted in Figure S8C. It shows the maximum amplitude of the +1-diffraction order is eight times and fifty times stronger than the amplitude for the -1- and zero-diffraction order, respectively. The results verify the concept that the proposed nonlinear metasurface can not only be used for VUV focusing, but also for realizing other important functionalities on demand in the future.

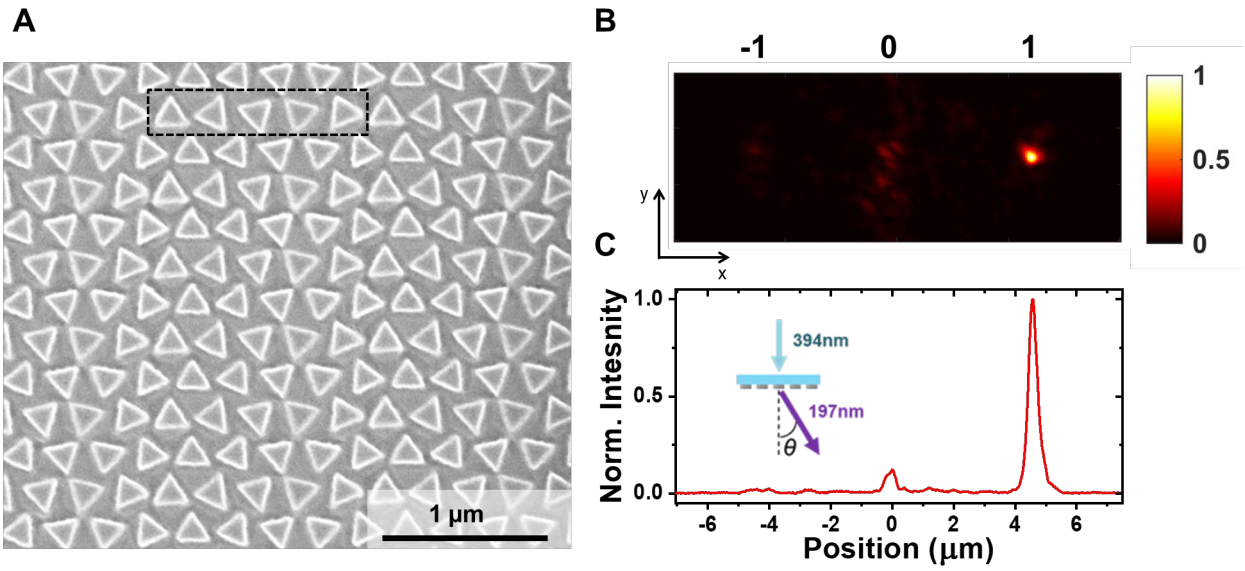

Fig. S10. Nonlinear beam steering. (A) SEM image of the beam-steering metasurface. The highlighted region indicates one supercell of this metasurface. (B) Section of the far-field diffraction pattern of the SHG signal. (C) Cross-sectional profile of the data shown in (B) along the x-axis through the highest intensity point.

Section VII: Effect of the substrate refractive index and meta-atom surface roughness on the VUV signal

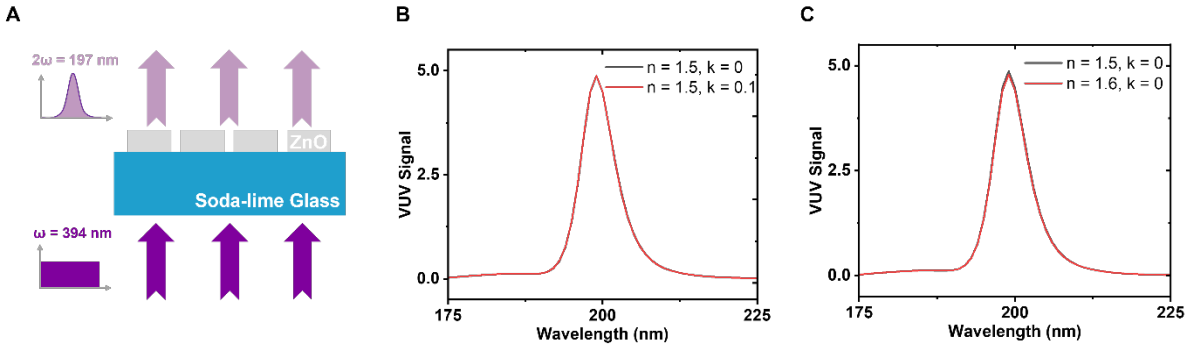

Fig. S11. Impact of substrate materials on the metalens' VUV signal. (a) Schematic of the excitation of SHG in the metalens. (a) Comparison between the nonlinear spectra of the reported ZnO metalens on a non-

absorptive substrate and an absorptive substrate. (b) Comparison between the nonlinear spectra of the reported ZnO metalens on substrates of different refractive indices.

The minimal impact of a VUV absorbing substrate is shown in Figure S11. The simulation assumes the VUV light is generated within the ZnO resonators and passes through free space rather than the absorbing glass substrate. This simulation matches our experimental conditions: excitation incident on the substrate side of the sample and VUV light generation on the opposite side leading to VUV light propagating in free space.

On the other hand, the surface roughness of meta-atom plays an important role in SHG due to the resonance shift introduced by the change of meta-atom's geometric shape. The impact of ZnO surface roughness on metalens' VUV signal is shown in Figure S12. The simulated surface roughness introduces a phase shift difference of ~20 degrees. A signal magnitude fluctuation of ~10% was also observed in the same simulation.

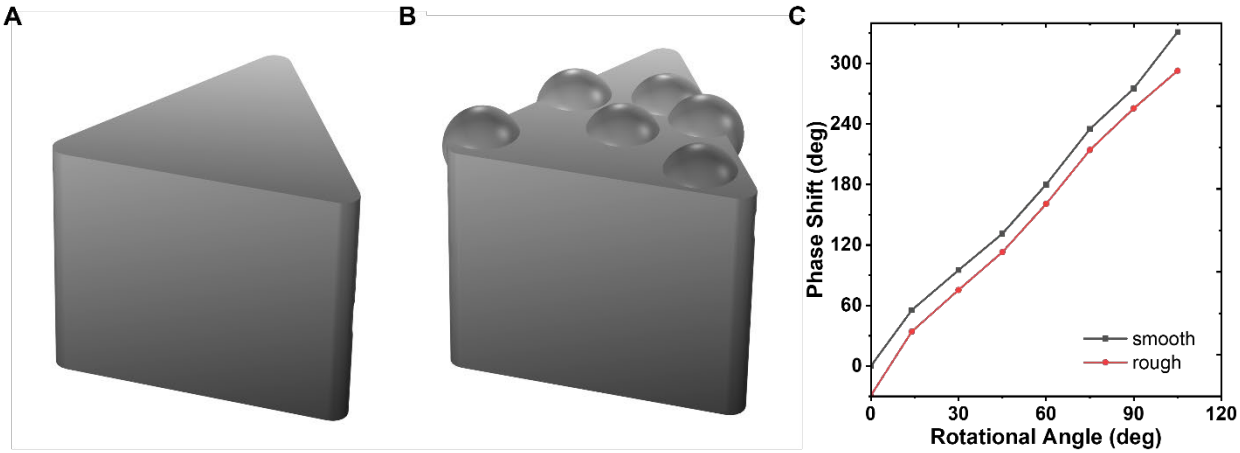

Fig. S12. Impact of meta-atom surface roughness on the metalens' VUV signal. (a) Smooth meta-atom. (b) Rough meta-atom. The surface roughness is simulated as spheres 24nm in radius with center buried 10nm below the meta-atom's upper surface. (c) Comparison between the phase shift of the two meta-atoms under different rotation.

REFERENCES AND NOTES

1. L.-H. Lai, D.-C. Che, K. Liu, Photodissociative pathways of C_2H_2 at 121.6 nm revealed by a Doppler-selected time-of-flight (a 3-D mapping) technique. *J. Phys. Chem.* **100**, 6376–6380 (1996).

2. S. Leach, H.-W. Jochims, H. Baumgärtel, VUV Photodissociation of ammonia: A dispersed fluorescence excitation spectral study. *Phys. Chem. Chem. Phys.* **7**, 900–911 (2005).

3. S. Lerouge, A. C. Fozza, M. R. Wertheimer, R. Marchand, L. H. Yahia, Sterilization by low-pressure plasma: The role of vacuum-ultraviolet radiation. *Plasmas Polym.* **5**, 31–46 (2000).

4. J. A. Sobota, S. Yang, J. G. Analytis, Y. L. Chen, I. R. Fisher, P. S. Kirchmann, Z. X. Shen, Ultrafast optical excitation of a persistent surface-state population in the topological insulator Bi_2Se_3. *Phys. Rev. Lett.* **108**, 117403 (2012).

5. V. N. Vasilets, A. V. Kuznetsov, V. I. Sevastianov, Vacuum ultraviolet treatment of polyethylene to change surface properties and characteristics of protein adsorption. *J. Biomed. Mater. Res. A* **69A**, 428–435 (2004).

6. Y. Mao, D. Zhao, S. Yan, H. Zhang, J. Li, K. Han, X. Xu, C. Guo, L. Yang, C. Zhang, K. Huang, Y. Chen, A vacuum ultraviolet laser with a submicrometer spot for spatially resolved photoemission spectroscopy. *Light Sci. Appl.* **10**, 22 (2021).

7. P. Bergonzo, U. Kogelschatz, I. W. Boyd, Direct photo-deposition of silicon dioxide films using a xenon excimer lamp. *Appl. Surf. Sci.* **69**, 393–397 (1993).

8. J. Wang, Z. Wang, F. Liu, L. Cai, J. B. Pan, Z. Li, S. Zhang, H. Y. Chen, X. Zhang, Y. Mo, Vacuum ultraviolet laser desorption/ionization mass spectrometry imaging of single cells with submicron craters. *Anal. Chem.* **90**, 10009–10015 (2018).

9. T. Ito, in *Synchrotron Radiation in Structural Biology*, R. M. Sweet, A. D. Woodhead, Eds. (Springer US, 1989), pp. 221–241.

10. M. Zelikoff, K. Watanabe, E. C. Y. Inn, Absorption coefficients of gases in the vacuum ultraviolet. Part II. Nitrous oxide. *J. Chem. Phys.* **21**, 1643–1647 (1953).

11. A. H. Kung, J. F. Young, S. E. Harris, Generation of 1182-Å radiation in phase-matched mixtures of inert gases. *Appl. Phys. Lett.* **22**, 301–302 (1973).

12. R. Miles, S. Harris, Optical third-harmonic generation in alkali metal vapors. *IEEE J. Quantum Electron.* **9**, 470–484 (1973).

13. D. E. Couch, D. D. Hickstein, D. G. Winters, S. J. Backus, M. S. Kirchner, S. R. Domingue, J. J. Ramirez, C. G. Durfee, M. M. Murnane, H. C. Kapteyn, Ultrafast 1 MHz vacuum-ultraviolet source via highly cascaded harmonic generation in negative-curvature hollow-core fibers. *Optica* **7**, 832–837 (2020).

14. P. S. Halasyamani, J. M. Rondinelli, The must-have and nice-to-have experimental and computational requirements for functional frequency doubling deep-UV crystals. *Nat. Commun.* **9**, 2972 (2018).

15. L. Koller, *Ultraviolet Radiation* (John Wiley & Sons, ed. 2, 1965).

16. V. Kildishev Alexander, A. Boltasseva, M. Shalaev Vladimir, Planar photonics with metasurfaces. *Science* **339**, 1232009 (2013).

17. I. Kuznetsov Arseniy, E. Miroshnichenko Andrey, L. Brongersma Mark, S. Kivshar Yuri, B. Luk'yanchuk, Optically resonant dielectric nanostructures. *Science* **354**, eaag2472 (2016).

18. G.-Y. Lee, J. Sung, B. Lee, Metasurface optics for imaging applications. *MRS Bull.* **45**, 202–209 (2020).

19. N. Yu, F. Capasso, Flat optics with designer metasurfaces. *Nat. Mater.* **13**, 139–150 (2014).

20. M. L. Tseng, Y. Jahani, A. Leitis, H. Altug, Dielectric metasurfaces enabling advanced optical biosensors. *ACS Photonics* **8**, 47–60 (2021).

21. S. M. Kamali, E. Arbabi, A. Arbabi, A. Faraon, A review of dielectric optical metasurfaces for wavefront control. *Nanophotonics* **7**, 1041–1068 (2018).

22. M. L. Tseng, H. H. Hsiao, C. H. Chu, M. K. Chen, G. Sun, A. Q. Liu, D. P. Tsai, Metalenses: Advances and applications. *Adv. Opt. Mater.* **6**, 1800554 (2018).

23. J. Engelberg, U. Levy, The advantages of metalenses over diffractive lenses. *Nat. Commun.* **11**, 1991 (2020).

24. K. Huang, F. Qin, H. Liu, H. Ye, C. W. Qiu, M. Hong, B. Luk'yanchuk, J. Teng, Planar diffractive lenses: Fundamentals, functionalities, and applications. *Adv. Mater.* **30**, 1704556 (2018).

25. R. J. Lin, V. C. Su, S. Wang, M. K. Chen, T. L. Chung, Y. H. Chen, H. Y. Kuo, J. W. Chen, J. Chen, Y. T. Huang, J. H. Wang, C. H. Chu, P. C. Wu, T. Li, Z. Wang, S. Zhu, D. P. Tsai, Achromatic metalens array for full-colour light-field imaging. *Nat. Nanotechnol.* **14**, 227–231 (2019).

26. S. Wang, P. C. Wu, V. C. Su, Y. C. Lai, M. K. Chen, H. Y. Kuo, B. H. Chen, Y. H. Chen, T. T. Huang, J. H. Wang, R. M. Lin, C. H. Kuan, T. Li, Z. Wang, S. Zhu, D. P. Tsai, A broadband achromatic metalens in the visible. *Nat. Nanotechnol.* **13**, 227–232 (2018).

27. M. K. Chen, Y. Wu, L. Feng, Q. Fan, M. Lu, T. Xu, D. P. Tsai, Principles, functions, and applications of optical meta-lens. *Adv. Opt. Mater.* **9**, 2001414 (2021).

28. C. H. Chu, M. L. Tseng, J. Chen, P. C. Wu, Y. H. Chen, H. C. Wang, T. Y. Chen, W. T. Hsieh, H. J. Wu, G. Sun, D. P. Tsai, Active dielectric metasurface based on phase-change medium. *Laser Photonics Rev.* **10**, 986–994 (2016).

29. A. Leitis, A. Heßler, S. Wahl, M. Wuttig, T. Taubner, A. Tittl, H. Altug, All-dielectric programmable Huygens' metasurfaces. *Adv. Funct. Mater.* **30**, 1910259 (2020).

30. M. L. Tseng, J. Yang, M. Semmlinger, C. Zhang, P. Nordlander, N. J. Halas, Two-dimensional active tuning of an aluminum plasmonic array for full-spectrum response. *Nano Lett.* **17**, 6034–6039 (2017).

31. P. C. Wu, R. A. Pala, G. Kafaie Shirmanesh, W. H. Cheng, R. Sokhoyan, M. Grajower, M. Z. Alam, D. Lee, H. A. Atwater, Dynamic beam steering with all-dielectric electro-optic III–V multiple-quantum-well metasurfaces. *Nat. Commun.* **10**, 3654 (2019).

32. J. Li, S. Kamin, G. Zheng, F. Neubrech, S. Zhang, N. Liu, Addressable metasurfaces for dynamic holography and optical information encryption. *Sci. Adv.*. **4**, eaar6768 (2018).

33. J. Cambiasso, G. Grinblat, Y. Li, A. Rakovich, E. Cortés, S. A. Maier, Bridging the gap between dielectric nanophotonics and the visible regime with effectively lossless gallium phosphide antennas. *Nano Lett.* **17**, 1219–1225 (2017).

34. K. Konishi, T. Higuchi, J. Li, J. Larsson, S. Ishii, M. Kuwata-Gonokami, Polarization-controlled circular second-harmonic generation from metal hole arrays with threefold rotational symmetry. *Phys. Rev. Lett.* **112**, 135502 (2014).

35. J. Lee, M. Tymchenko, C. Argyropoulos, P. Y. Chen, F. Lu, F. Demmerle, G. Boehm, M. C. Amann, A. Alù, M. A. Belkin, Giant nonlinear response from plasmonic metasurfaces coupled to intersubband transitions. *Nature* **511**, 65–69 (2014).

36. S. Liu, P. P. Vabishchevich, A. Vaskin, J. L. Reno, G. A. Keeler, M. B. Sinclair, I. Staude, I. Brener, An all-dielectric metasurface as a broadband optical frequency mixer. *Nat. Commun.* **9**, 2507 (2018).

37. P. N. Melentiev, A. E. Afanasiev, A. A. Kuzin, V. M. Gusev, O. N. Kompanets, R. O. Esenaliev, V. I. Balykin, Split hole resonator: A nanoscale UV light source. *Nano Lett.* **16**, 1138–1142 (2016).

38. M. Semmlinger, M. L. Tseng, J. Yang, M. Zhang, C. Zhang, W. Y. Tsai, D. P. Tsai, P. Nordlander, N. J. Halas, Vacuum ultraviolet light-generating metasurface. *Nano Lett.* **18**, 5738–5743 (2018).

39. M. Semmlinger, M. Zhang, M. L. Tseng, T. T. Huang, J. Yang, D. P. Tsai, P. Nordlander, N. J. Halas, Generating third harmonic vacuum ultraviolet light with a TiO_2 metasurface. *Nano Lett.* **19**, 8972–8978 (2019).

40. G. Li, S. Zhang, T. Zentgraf, Nonlinear photonic metasurfaces. *Nat. Rev. Mater.* **2**, 17010 (2017).

41. H. J. Simon, N. Bloembergen, Second-harmonic light generation in crystals with natural optical activity. *Phys. Rev.* **171**, 1104–1114 (1968).

42. T. Kaelberer, V. A. Fedotov, N. Papasimakis, D. P. Tsai, N. I. Zheludev, Toroidal dipolar response in a metamaterial. *Science* **330**, 1510–1512 (2010).

43. K. Watanabe, M. Zelikoff, E. C. Inn, "Absorption coefficients of several atmospheric gases," (Air Force Cambridge Research Labs Hanscom AFB MA, 1953).

44. J. H. Park, S. J. Jang, S. S. Kim, B. T. Lee, Growth and characterization of single crystal ZnO thin films using inductively coupled plasma metal organic chemical vapor deposition. *Appl. Phys. Lett.* **89**, 121108 (2006).

45. L. Wang, S. Kruk, K. Koshelev, I. Kravchenko, B. Luther-Davies, Y. Kivshar, Nonlinear wavefront control with all-dielectric metasurfaces. *Nano Lett.* **18**, 3978–3984 (2018).

46. T. Pertsch, Y. Kivshar, Nonlinear optics with resonant metasurfaces. *MRS Bull.* **45**, 210–220 (2020).

47. C. Schlickriede, S. S. Kruk, L. Wang, B. Sain, Y. Kivshar, T. Zentgraf, Nonlinear imaging with all-dielectric metasurfaces. *Nano Lett.* **20**, 4370–4376 (2020).

48. T. Hu, C. K. Tseng, Y. H. Fu, Z. Xu, Y. Dong, S. Wang, K. H. Lai, V. Bliznetsov, S. Zhu, Q. Lin, Y. Gu, Demonstration of color display metasurfaces via immersion lithography on a 12-inch silicon wafer. *Opt. Express* **26**, 19548–19554 (2018).

49. A. Leitis, M. L. Tseng, A. John-Herpin, Y. S. Kivshar, H. Altug, Wafer-scale functional metasurfaces for mid-infrared photonics and biosensing. *Adv. Mater.* **33**, 2102232 (2021).

50. C. H. Zhai, R. J. Zhang, X. Chen, Y. X. Zheng, S. Y. Wang, J. Liu, N. Dai, L. Y. Chen, Effects of Al doping on the properties of ZnO thin films deposited by atomic layer deposition. *Nanoscale Res. Lett.* **11**, 407 (2016).

51. K. O'Brien, H. Suchowski, J. Rho, A. Salandrino, B. Kante, X. Yin, X. Zhang, Predicting nonlinear properties of metamaterials from the linear response. *Nat. Mater.* **14**, 379–383 (2015).

52. B. H. Chen, P. C. Wu, V. C. Su, Y. C. Lai, C. H. Chu, I. C. Lee, J. W. Chen, Y. H. Chen, Y. C. Lan, C. H. Kuan, D. P. Tsai, GaN metalens for pixel-level full-color routing at visible light. *Nano Lett.* **17**, 6345–6352 (2017).

53. M. L. Tseng, Z. H. Lin, H. Y. Kuo, T. T. Huang, Y. T. Huang, T. L. Chung, C. H. Chu, J. S. Huang, D. P. Tsai, Stress-induced 3D Chiral fractal metasurface for enhanced and stabilized broadband near-field optical chirality. *Adv. Opt. Mater.* **7**, 1900617 (2019).

54. P. C. Wu, W. L. Hsu, W. T. Chen, Y. W. Huang, C. Y. Liao, A. Q. Liu, N. I. Zheludev, G. Sun, D. P. Tsai, Plasmon coupling in vertical split-ring resonator metamolecules. *Sci. Rep.* **5**, 9726 (2015).

55. P. J. Campagnola, A. C. Millard, M. Terasaki, P. E. Hoppe, C. J. Malone, W. A. Mohler, Three-dimensional high-resolution second-harmonic generation imaging of endogenous structural proteins in biological tissues. *Biophys. J.* **82**, 493–508 (2002).

56. S. Sun, K. Y. Yang, C. M. Wang, T. K. Juan, W. T. Chen, C. Y. Liao, Q. He, S. Xiao, W. T. Kung, G. Y. Guo, L. Zhou, D. P. Tsai, High-efficiency broadband anomalous reflection by gradient meta-surfaces. *Nano Lett.* **12**, 6223–6229 (2012).